

1 **REVISION 2**

2 **Morin-type transition in 5C pyrrhotite**

3 C R S Haines<sup>1\*</sup>, G I Lampronti<sup>1</sup>, W T Klooster<sup>2</sup>, S J Coles<sup>2</sup>, S E Dutton<sup>3</sup>, and M A Carpenter<sup>1</sup>

4 *<sup>1</sup>Department of Earth Sciences, University of Cambridge, Cambridge, UK*

5 *<sup>2</sup>UK National Crystallographic Service, Chemistry, Faculty of*

6 *Natural and Environmental Sciences,*

7 *University of Southampton, SO17 1BJ, UK*

8 *<sup>3</sup>Department of Physics, University of Cambridge, Cambridge, UK*

9 **Abstract**

10 We report the discovery of a low temperature spin-flop transition in 5C pyrrhotite at ~155 K  
11 that is similar to those seen in hematite at 260 K and FeS (troilite) at 440 K. The 5C crystal was  
12 produced by annealing a 4C pyrrhotite crystal at 875 K, to produce a change in the vacancy-  
13 ordering scheme that developed during cooling. The 5C structure is confirmed by single crystal x-  
14 ray diffraction and the stoichiometry and homogeneity by electron microprobe and SEM BSE  
15 mapping. RUS, heat capacity and magnetisation measurements from room temperature down to 2  
16 K are reported. The transition is marked by a steep change in elastic properties at the transition  
17 temperature, a peak in the heat capacity and weak anomalies in measurements of magnetisation.  
18 Magnetic hysteresis loops and comparison with the magnetic properties of 4C pyrrhotite suggest  
19 that the transition involves a change in orientation of moments between two different  
20 antiferromagnetic structures, perpendicular to the crystallographic *c*-axis at high temperatures and  
21 parallel to the crystallographic *c*-axis at low temperatures. The proposed structures are consistent

22 with a group theoretical treatment that also predicts a first order transition between the magnetic  
23 structures.

## 24 I. INTRODUCTION

25 The pyrrhotite system comprises a number of related structures having compositions  $\text{Fe}_{1-x}\text{S}$   
26 where  $0 < x < 0.125$ . The best known of these structures are troilite ( $\text{FeS}$ ) and 4C pyrrhotite  
27 ( $\text{Fe}_7\text{S}_8$ ). 4C is so called because it is a superstructure with a 4 cell repeat along the  $c$ -axis with  
28 respect to the parent NiAs structure (Bertaut 1953; Powell 2004). Other commensurate  
29 superstructures have been reported as 3C (Fleet 1971, Nakano et al 1979), 5C (de Villiers et al  
30 2009, Elliot 2010, Liles and de Villiers 2012) and 6C (Koto et al 1975, de Villiers and Liles 2010),  
31 while some are incommensurate (Nakazawa and Morimoto 1971, Morimoto et al 1975, Yamamoto  
32 and Nakazawa 1982, Izaola et al 2007). Ferrimagnetic pyrrhotite (4C) is an important carrier of  
33 magnetic remanence on earth and possibly also on Mars (e.g. Martin-Hernandez et. al 2008;  
34 Rochette et. al 2005), but 4C structures are not unique and the other superstructure types have  
35 different structure/property relationships which are much less well known. The key issue in  
36 relation to the magnetic structures are how vacancies order on the cation sites as the stoichiometry  
37 changes and how the distribution of vacancies then controls the magnetic structures.

38 By adopting a group theoretical approach, Haines et al. (2019a) have shown that the  
39 commensurate superstructures of pyrrhotite, which have different Fe/vacancy ordering schemes,  
40 are all likely to undergo a magnetically driven spin reorientation transition with accompanying  
41 small distortions of the crystal lattice at low temperatures. The prediction for the case of 5C  
42 pyrrhotite is for an abrupt spin-flop transition similar to the Morin transition in hematite. The  
43 present work focuses on the magnetic and elastic properties of a natural 4C crystal that transformed  
44 unexpectedly to 5C crystal after being heated above its concomitant vacancy ordering and Néel  
45 temperature of 595 K. We report a newly identified magnetic transition at  $\sim 155$  K in the 5C crystal  
46 and propose that it is a spin-flop transition between two antiferromagnetic structures, with an

47 origin that is closely related to that of the magnetic transitions already known in FeS at 440 K and  
48 4C Fe<sub>7</sub>S<sub>8</sub> at 35 K.

49 In general, 5C pyrrhotite is found to have a composition close to Fe<sub>9</sub>S<sub>10</sub>. However, Pósfai et.  
50 al. (2000) reported a 5C polytype with composition Fe<sub>7</sub>S<sub>8</sub>. Kontny et. al. (2000) also presented  
51 some x-ray diffraction and magnetisation measurements on multiphase samples, suggesting the  
52 possibility of pyrrhotite with a 5C structure having the stoichiometry close to the Fe<sub>7</sub>S<sub>8</sub> that is  
53 usually associated with the 4C structure. De Villiers et al. (2009) proposed space group number  
54 63 *Cmce* (formerly *Cmca*) as the correct crystallographic space group at room temperature. Elliot  
55 (2010) had claimed *P2<sub>1</sub>/c* for the room temperature structure. Liles and de Villiers (2012)  
56 subsequently proposed *P2<sub>1</sub>* for the structure at both room temperature and 120 K. There do not  
57 appear to have been any studies of the magnetic structure.

58 In this work, we first establish the stoichiometry of the sample through electron microprobe  
59 analysis before going on to present a structural solution in the space group 63 *Cmce* based on  
60 single crystal diffraction data collected on a single crystal sample of 5C pyrrhotite at room  
61 temperature. We then present heat capacity, DC magnetisation and resonant ultrasound  
62 spectroscopy (RUS) measurements on a second single crystal over the range 2-300 K.

## 63 **II. SAMPLE PREPARATION**

64 The single crystal sample of pyrrhotite used in this study was cut from a cm-sized crystal in the  
65 mineral collection of the South Australia Museum that had originated from a mine in Mexico.  
66 Samples from the same parent crystal have been described in Haines et al (2019c). At the start, it  
67 was nearly in the shape of a rectangular parallelepiped with two pairs of parallel faces 1.7 mm and  
68 1.5 mm apart and a third pair of non-parallel faces separated by between 1 mm and 1.5mm. The  
69 first experiment was to collect RUS spectra through the temperature interval 10 - 295 K to confirm

70 that it was 4C pyrrhotite with a Besnus transition (Bensus and Meyer 1964) at  $\sim 35$  K (see Haines  
71 et al. 2019b).

72 After removal from the RUS instrument, the crystal was heated slowly to 875 K in flowing  
73 argon, with an oxygen trap, over four and a half days before cooling it back to room temperature  
74 over three days. The sample was held between two alumina rods. The heating and cooling rates  
75 through the 595 K transition were 2.2 K/hour. As a consequence of this treatment, the crystal  
76 acquired a thin oxide layer that was removed mechanically, and also broke into two pieces. The  
77 larger piece had a mass of  $9.1 \pm 0.1$  mg and was used for heat capacity, magnetisation and RUS  
78 measurements. On completion of these measurements, the larger piece was mounted and  
79 polished for chemical analysis. The smaller piece weighed  $2.2 \pm 0.1$  mg and was broken up for  
80 the single crystal diffraction measurements.

### 81 **III. ELECTRON MICROPROBE ANALYSIS**

82 Chemical analysis on the larger piece was carried out using a Cameca SX100 electron  
83 microprobe in the Department of Earth Sciences, University of Cambridge (instrumental  
84 conditions: 20 keV, 10 nA,  $1 \mu\text{m}$  beam diameter). With respect to 10 sulphur atoms, the average  
85 of 20 analyses gave the number of Fe atoms as  $9.21 \pm 0.05$ . Co, Cu, Mn, Ni and Zn were measured  
86 for, but all were below the detection limit on all of the 20 analysis spots. We highlight here that  
87 this shows a significant change in stoichiometry from the parent crystal described in Haines et al.  
88 (2019c) in which electron microprobe analysis revealed a homogeneous and pure 4C crystal of  
89 stoichiometry 7.00(6) Fe atoms per 8 sulphur atoms. We suggest that this change of stoichiometry  
90 is due to the loss of sulphur from the crystal rather than the addition of iron for which no source  
91 or mechanism is present. To check for zoning or inhomogeneity in the stoichiometry of the crystal  
92 a scanning electron microscope back-scattered electron (SEM-BSE) analysis map of nearly the  
93 whole surface of the same piece used for the electron microprobe analysis was collected. The

94 SEM-BSE map showed no sign of any chemical inhomogeneity above the level of detection. We  
95 therefore conclude that the transformation from stoichiometry  $\text{Fe}_{7.00(6)}\text{S}_8$  to  $\text{Fe}_{9.21(5)}\text{S}_{10}$  is  
96 complete and homogeneous. The images are included as supplemental information (SI 2020).

97

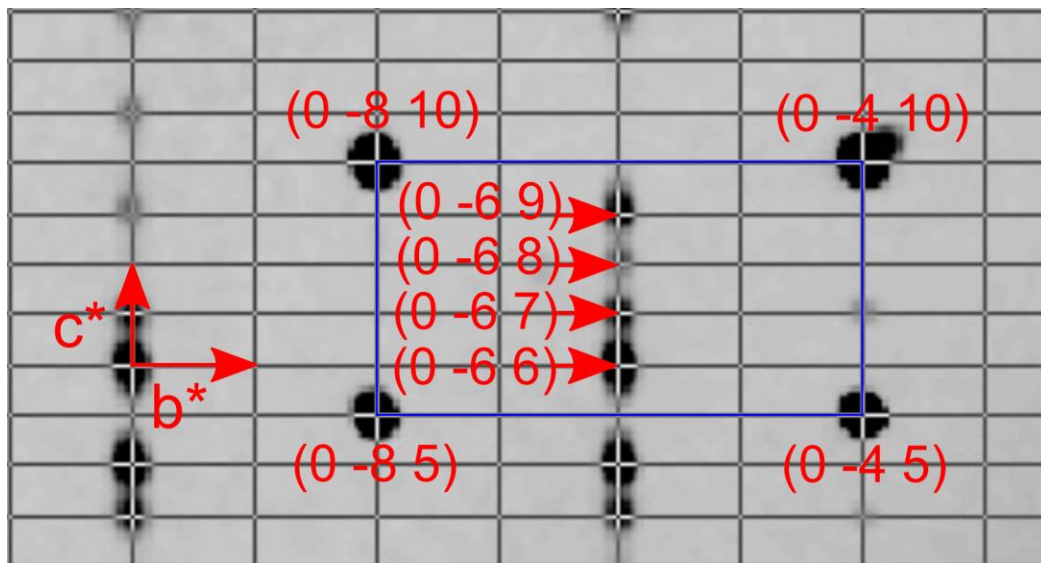
#### 98 **IV. SINGLE CRYSTAL X-RAY DIFFRACTION**

99 The single crystal used for X-ray diffraction was black and plate-shaped, with dimensions  
100  $\sim 0.080 \times 0.040 \times 0.020 \text{ mm}^3$ . It was mounted on a MITIGEN holder in perfluoroether oil on a  
101 Rigaku FRE+ diffractometer equipped with VHF Varimax confocal mirrors and an AFC12  
102 goniometer and HyPix 6000HE detector. The temperature was  $293 \pm 2 \text{ K}$  during scans of  $0.5^\circ$  per  
103 frame for 1.3 s with Mo K radiation (Rotating-anode X-ray tube, 40 kV, 30 mA). The total number  
104 of runs and images was based on the strategy calculation from the program CrysAlisPro (Rigaku,  
105 V1.171.39.46, 2018). The maximum resolution achieved was at  $27.478^\circ$  ( $0.77 \text{ \AA}$ ). Cell parameters  
106 were retrieved using the CrysAlisPro (Rigaku, V1.171.39.46, 2018) software and refined using  
107 CrysAlisPro (Rigaku, V1.171.39.46, 2018) on 5787 reflections, 22% of the observed reflections.  
108 Data reduction, scaling and absorption corrections were performed using CrysAlisPro (Rigaku,  
109 V1.171.39.46, 2018). The final completeness is 99.7 % out to  $25^\circ$  in  $\Theta$ . A multi-scan absorption  
110 correction was performed using CrysAlisPro 1.171.39.46 (Rigaku Oxford Diffraction, 2018) using  
111 spherical harmonics as implemented in SCALE3 ABSPACK. The absorption coefficient of this  
112 material is  $13.664 \text{ mm}^{-1}$  at this wavelength ( $= 0.711 \text{ \AA}$ ) and the minimum and maximum  
113 transmissions are 0.522 and 1.000.

114 Figure 1 shows a section of the  $(0kl)$  plane of the diffraction pattern, with 5 superlattice  
115 reflections clearly visible along the  $c^*(k_z)$  of the parent NiAs cell. We looked for evidence of  
116 incommensuration by initially indexing the pattern with the NiAs unit cell and then using an  
117 incommensurate k-vector to describe the remaining peaks. The k-vector which describes the

118 pattern has components of 0.500(3) along the planar hexagonal axes and 0.204(6) perpendicular  
119 to the ab-plane of the parent structure. This is therefore commensurate within experimental  
120 uncertainty.

121



122

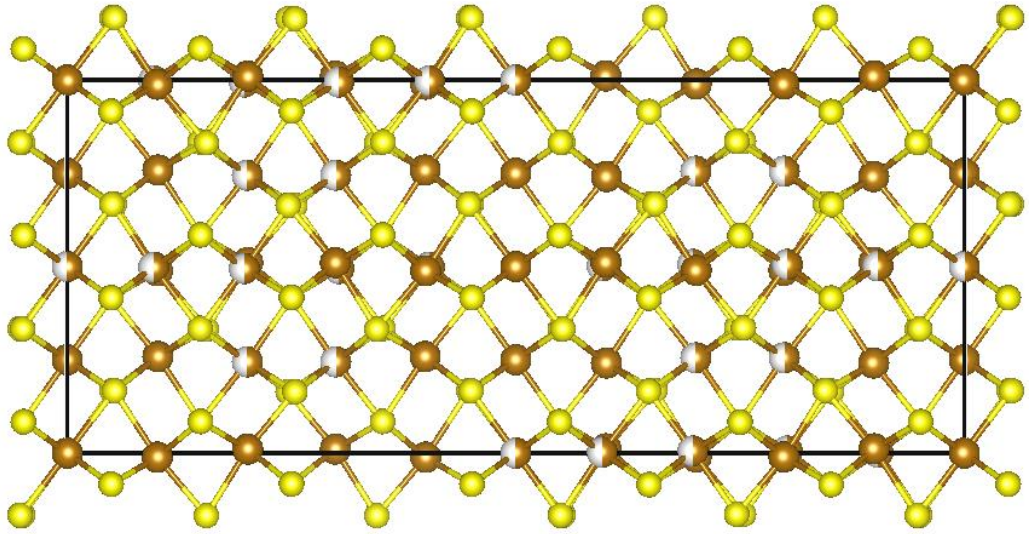
123 Figure 1. Part of the  $(0kl)$  precession image of the room temperature single crystal X-ray  
124 diffraction pattern, showing the five-fold superlattice reflections of the 5C structure. The data has  
125 been reduced using the cell from the  $Cmce$  structure and the peaks are labelled with the  $(hkl)$  of  
126 the  $Cmce$  structure. The direction of the  $b^*$  and  $c^*$  are given in red on the left. The unit cell of the  
127  $Cmce$  structure is shown by the grey grid. The projection of the hexagonal parent cell onto the  
128  $Cmce$   $(0kl)$  plane is shown in blue. The five-fold modulation in the  $l$  direction can be seen and the  
129 peaks characteristic of this are labelled with their  $(hkl)$  values.

130

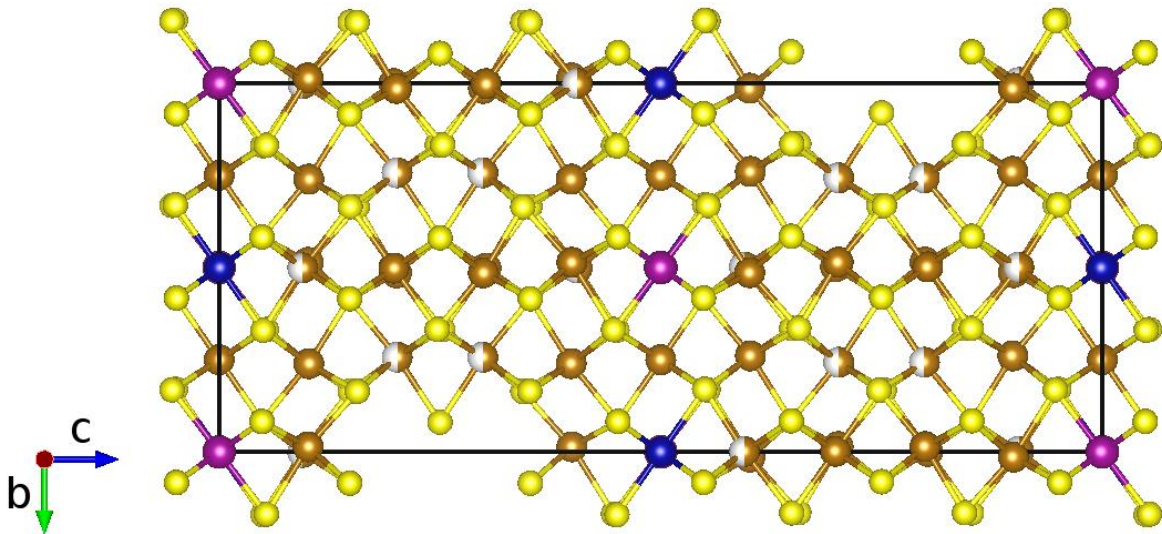
131 The structural solution and subsequent refinement were undertaken using the SHELXS  
132 program (Sheldrick 1997), proceeding with 9 Fe and 8 S atomic positions. Neutral scattering  
133 factors were used for all atoms. The appropriate 3-individual twin matrix describing a 120°  
134 rotation along the c axis was introduced in the first stages of the refinement; since the three  
135 individual fractions were found to be all close to 33%, this step was necessary to take the  
136 discrepancy factor  $R1$  below 0.2. Individual occupancy factors for the Fe atoms were refined with  
137 an overall isotropic thermal parameter to detect the partially vacant sites. The Fe sites that refined  
138 to occupancies close to 1.0 were then fixed at unity, and the thermal displacement parameters were  
139 then refined independently. Lastly, the ADPs were refined anisotropically, together with the  
140 occupancies of the four partially vacant Fe atoms. Because of an unreasonably prolate ADP for  
141 the atom at (0,0,0) Fe9 the thermal displacement parameters were restrained to be similar to those  
142 of the neighbour Fe sites. We here highlight that this is not the same position found to be vacant  
143 in the structural refinement performed by De Villiers et al. (2009), corresponding to Fe4 in our  
144 model. Details of the structural solutions are given in the accompanying cif file.

145 The refinement converged with a discrepancy factor  $R1 = 0.0485$  for 1675 observed reflections  
146 and  $R1 = 0.0604$  for all 2084 measured reflections and 120 parameters. The goodness of fit  
147 parameter was  $S = 1.476$  and  $wR2$  was 0.3431. No extinction correction parameter was used as it  
148 was found to converge to zero. The largest residual electron density amounted to 1.32 e/Å.  
149 Interestingly, the structural model reported by De Villiers et al. (2009) also differs in the way the  
150 Fe planes stack along the [001] direction (see Figure 2).





151



152

153

154 Figure 2. Structural model of pyrrhotite 5C viewed along [100] from this work (top) and from de

155 Villiers et al. (2009) (bottom). Color code: yellow = S sites; brown = Fe sites (partial occupancy

156 is shown by half-grey half-brown); pink = partially Ni replaced Fe site (De Villiers et al., 2009);

157 blue = vacant metal site from De Villiers et al. (2009) (see main text for details).

158

159 The composition, calculated from the refinement of the structure, is  $\text{Fe}_{9.22(1)}\text{S}_{10}$ , in excellent  
 160 agreement with the results of the electron microprobe analysis. Details of the refinement and the  
 161 comparison to that of De Villiers et al. (2009) are given in Table 1. A cif file containing detailed  
 162 information about data collection and structural refinement is supplied separately.

163

164 Table 1. Crystal data and structure refinement details for 5C pyrrhotite.

	<i>This work</i>	<i>De Villiers et al. (2009)</i>
<i>Empirical formula</i>	$\text{Fe}_{9.22(1)}\text{S}_{10}$	$\text{Fe}_{8.79}\text{Ni}_{0.118}\text{S}_{10}$
<i>Formula weight</i>	6682.51	6588.86
<i>Temperature (°K)</i>	293(2)	293(2)
<i>Wavelength (Å)</i>	0.71073	0.71073
<i>Space group</i>	<i>Cmce</i> (formerly <i>Cmca</i> )	<i>Cmce</i> (formerly <i>Cmca</i> )
<i>Unit cell dimensions</i>	$a = 6.890(2) \text{ \AA}$ $b = 11.9436(4) \text{ \AA}$ $c = 28.7916(10) \text{ \AA}$ $\alpha = 90^\circ$ $\beta = 90^\circ$ $\gamma = 90^\circ$	$a = 6.893(3) \text{ \AA}$ $b = 11.939(3) \text{ \AA}$ $c = 28.635(15) \text{ \AA}$ $\alpha = 90^\circ$ $\beta = 90^\circ$ $\gamma = 90^\circ$
<i>Volume</i>	$2371.36(13) \text{ \AA}^3$	$2356.4(15) \text{ \AA}^3$
<i>Z, Calculated Density</i>	8, 4.689 g/cm <sup>3</sup>	8, 4.643 g/cm <sup>3</sup>
<i>Absorption coefficient</i>	12.681	12.516
<i>F(000)</i>	3358	3154
<i>Crystal size</i>	0.08x 0.04 x 0.02 mm <sup>3</sup>	0.14 x 0.06 x 0.03 mm <sup>3</sup>
<i><math>\theta</math> range for data collection</i>	2.12-31.82°	2.85-26.34°
<i>Limiting indices</i>	$-9 \leq h \leq 9, -16 \leq k \leq 15, -40 \leq l \leq 42$	$-8 \leq h \leq 7, -8 \leq k \leq 14, -33 \leq l \leq 29$
<i>Reflections collected/unique</i>	29278/2084 [R(int) = 0.0322]	6041/1264 [R(int) = 0.0322]
<i>Completeness to <math>\theta = 25.00</math></i>	99.7%	99.2%
<i>Refinement method</i>	Full-matrix least-squares on $F^2$	Full-matrix least-squares on $F^2$

<i>Data / restraints / parameters</i>	2084 / 1 / 120	1264 / 0 / 109
<i>Goodness-of-fit on F<sup>2</sup></i>	1.477	1.225
<i>Final R indices [I &gt; 2<math>\theta</math>(I)]</i>	R1 = 0.0485, wR2 = 0.3231	R1 = 0.0716, wR2 = 0.1513
<i>R indices (all data)</i>	R1 = 0.0604, wR2 = 0.3431	R1 = 0.0937, wR2 = 0.1627
<i>Extinctions coefficient</i>	-	0.00003(2)
<i>largest diff. peak and deepest hole</i>	1.445 and -1.346 e <sup>-</sup> ·Å <sup>-3</sup>	1.533 and -2.125 e <sup>-</sup> ·Å <sup>-3</sup>

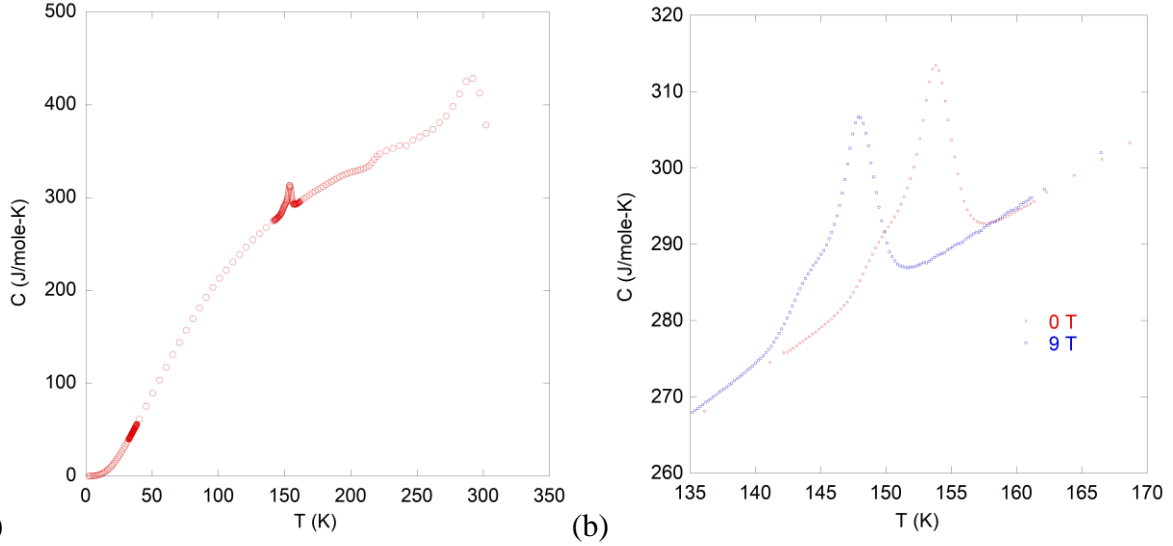
165

166

## 167 V. HEAT CAPACITY

168 Heat capacity measurements were carried out in a Quantum Design PPMS. The 9.1mg sample  
169 was fixed to the measurement platform of the heat capacity puck with Apiezon N grease. The puck  
170 (plus grease) was measured through the temperature interval 2-300 K with and without the sample  
171 to determine the background contribution needed to obtain the heat capacity of the sample alone.  
172 At low temperatures the heat capacity of the sample was larger than the background but at  
173 temperatures above ~30K the background was larger.

174 Figure 3a shows a peak in the heat capacity of the crystal near 155 K. Broad features at 215 K  
175 and 280 K are artefacts due to the Apiezon grease. A closer view of the peak (Fig. 3b) reveals it  
176 to be at 154 K with an apparent onset temperature of ~147 K and a tail up to ~157 K. Repeat  
177 measurements in a field of 9 T applied parallel to the [100] direction of the crystal (*H*//*a* of the  
178 NiAs cell) yielded a peak at 148 K (Fig. 3b). The shape of the peak was unchanged, but the  
179 transition had clearly been shifted down in temperature by ~6 K. There is no evidence in the data  
180 for the Besnus transition at 35 K, which confirms that the crystal had fully transformed from the  
181 4C structure. The peak is asymmetric. There is a shoulder on the low temperature side suggesting  
182 that there are two contributions to the peak. This is somewhat similar to the heat capacity anomaly  
183 recently observed in 4C pyrrhotite (Haines *et al.* 2019b).



184 (a) Heat capacity of 5C crystal measured between 2 and 300 K in zero field, showing  
 185 the magnetic transition near 155 K. Anomalies at ~215 and ~280 K are artefacts. (b) Higher  
 186 resolution view of the peak at 154 K in zero field, which shifts to 148 K when measured in a 9 T  
 187 field ( $H//a$ ).  
 188

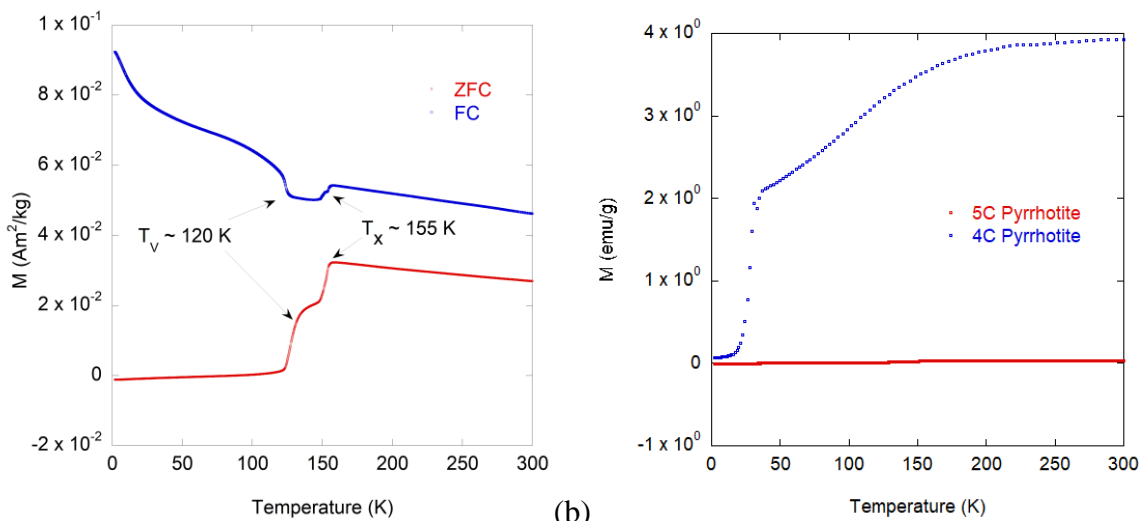
189  
 190 **VI. MAGNETISATION**

191 Magnetisation was measured using a Quantum Design MPMS. Zero field cooled (ZFC) data  
 192 were collected by cooling the crystal in zero applied field to 2 K before applying a 10 mT field  
 193 ( $H//a$ ) and measuring the moment in a continuous heating sweep up to 300 K at 3K/min. Field  
 194 cooled (FC) data were collected by cooling the crystal to 2 K in an applied field of 5 T before  
 195 removing the 5T field and applying a 10 mT field ( $H//a$ ) during measurements of the moment in  
 196 a continuous heating sweep up to 300 K at 3K/min. There are two distinct features observable in  
 197 both the ZFC and FC magnetisation curves, at ~120 and ~155 K. The feature at ~155 K cannot be  
 198 explained by any obvious impurity and matches up well with the transition seen in the heat capacity  
 199 of the 5C crystal. The feature at ~120 K is almost certainly from the Verwey transition of  
 200 magnetite, revealing the presence of a small amount of magnetite as an impurity phase. This is

201 most likely remaining from incomplete removal of the thin oxidised layer, following the heat  
 202 treatment at 875 K. The same crystal was used for both magnetisation and heat capacity  
 203 measurements, and the lack of any anomalies in the heat capacity at  $\sim 120$  K supports the  
 204 conclusion that the proportion of magnetite was very small.

205 In order to put the absolute values of magnetisation in context, results for the 5C crystal and for  
 206 a 4C crystal cut from the parent crystal temperature are compared in Figure 4b. 4C pyrrhotite is  
 207 ferrimagnetic, due to an uncompensated moment arising from the fact that one in eight Fe sites are  
 208 vacant. The measured moment of the 4C crystal at room temperature is a factor of  $\sim 100$  larger  
 209 than that of the 5C crystal, suggesting that the magnetic ground state of 5C pyrrhotite is a fully  
 210 compensated antiferromagnet. Furthermore, this puts an upper limit on the amount of 4C  
 211 pyrrhotite remaining in the sample of approximately 1%. In the ZFC data the step-like feature at  
 212 155 K takes place between 148 K and 155 K, with a midpoint of 152 K. The start stop and mid-  
 213 points of the step in the FC data are the same, though there is a small kink at the mid-point that is  
 214 not observed in the ZFC data.

215

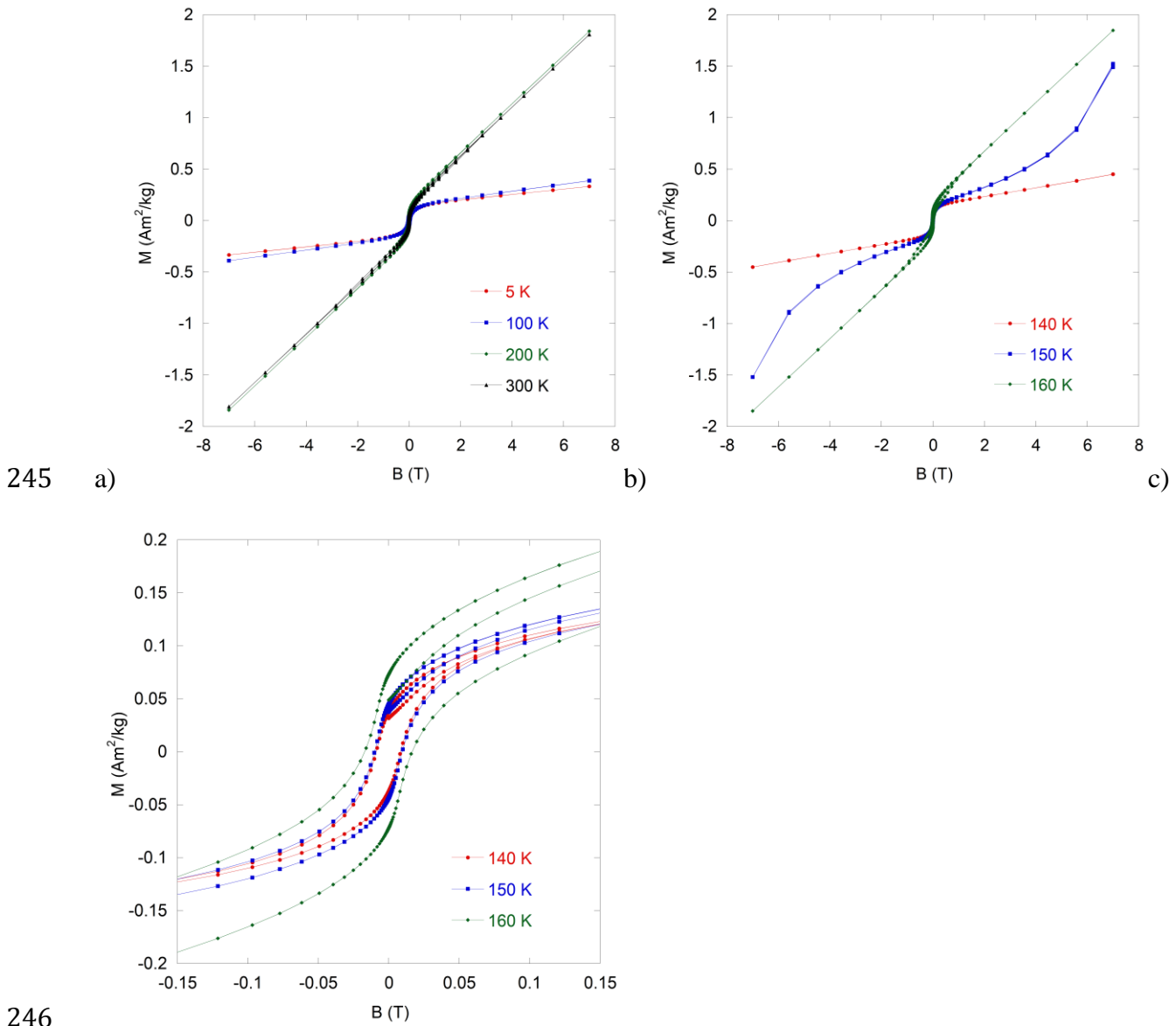


217 Figure 4. Magnetisation,  $M$ , of 5C crystal. (a) ZFC and FC data, measured in a field of 10 mT  
218 ( $H//a$ ). The anomaly at  $\sim 120$  K is due to the presence of a small amount of magnetite (labelled as  
219  $T_V$  for the Verwey transition) as impurity phase. The previously unknown transition is labelled as  
220  $T_x$ . (b) Comparison with ZFC data for 4C and 5 C crystals ( $H//a$ ), showing a difference in  
221 magnetisation of a factor of  $\sim 100$ .

222

223 Figure 5a contains hysteresis ( $M$ - $H$ ) loops measured between  $+7$  and  $-7$  T at two temperatures  
224 well above and two temperatures well below the magnetic transition. The values of  $M$  never exceed  
225  $\sim 2$  Am<sup>2</sup>/kg and are smaller at all fields by a factor of at least ten in comparison with the 4C  
226 structure (Powell et. al 2004; Charilou et. al 2015). They also show no indication of saturation at  
227 any temperature, consistent with antiferromagnetic structures. Above the transition, the  
228 magnetisation at 7 T (1.8 Am<sup>2</sup>/kg) is more than 4 times larger than it is below the transition (0.4  
229 Am<sup>2</sup>/kg) at the same field. Below 150 K, [100] is a relatively hard direction, but becomes relatively  
230 soft above  $\sim 150$  K. The difference remains marked even at 140 and 160 K, but there is a  
231 metamagnetic transition at 150 K from the low temperature magnetic structure, at low fields, to  
232 the high temperature structure at high fields (Fig. 5b). This is permissive of a first order spin-flop  
233 transition between two antiferromagnetic structures that have their moments aligned in the plane  
234 perpendicular to the  $c$ -axis above the transition point and parallel to the  $c$ -axis below it. In this  
235 scenario, small openings of the curves at low fields (Fig. 5c) and the small hysteresis seen in the  
236 magnetisation curves at all temperatures are attributed to the magnetite impurity identified on the  
237 basis of the magnetic anomaly at  $\sim 120$  K (Fig. 3a). In addition, the (near) saturation moment of  
238 these two impurities (at a field of 1.5 T) would limit their presence in the sample to similar values.  
239 If the entire signal at 300 K and 1.5 T were attributed to magnetite (this is around 0.5 Am<sup>2</sup>/kg) this  
240 would equate to 46  $\mu$ g of magnetite or 0.5% of the total mass, using a value of 90 Am<sup>2</sup>/kg for

241 saturation magnetisation of magnetite (Hunt et al. 2103 and references therein). In a similar way  
 242 we can constrain the 4C pyrrhotite to be less than 2.5% of the total mass (using 20 Am<sup>2</sup>/kg as the  
 243 value of the magnetisation from Hunt et al. (1995) and Haines et al (2019b).  
 244



247 Figure 5. (a) Field and temperature dependence of the magnetisation of the 5C sample. The  
 248 field was applied parallel to the [100] direction of the parent NiAs structure unit cell ( $H//a$ ). The  
 249 structure at 200 and 300 K has marked differences in magnetic anisotropy from the structure at 5

250 and 100 K. Neither show any indication of saturation at high fields. (b) Field and temperature  
251 dependence of magnetisation of the 5C structure close to the magnetic transition at  $\sim 155$  K ( $H//a$ ).  
252 (c) Close in view of the low field region from (b), showing slight opening of the loops that is  
253 attributed to the presence of a small amount of magnetite.

254

255

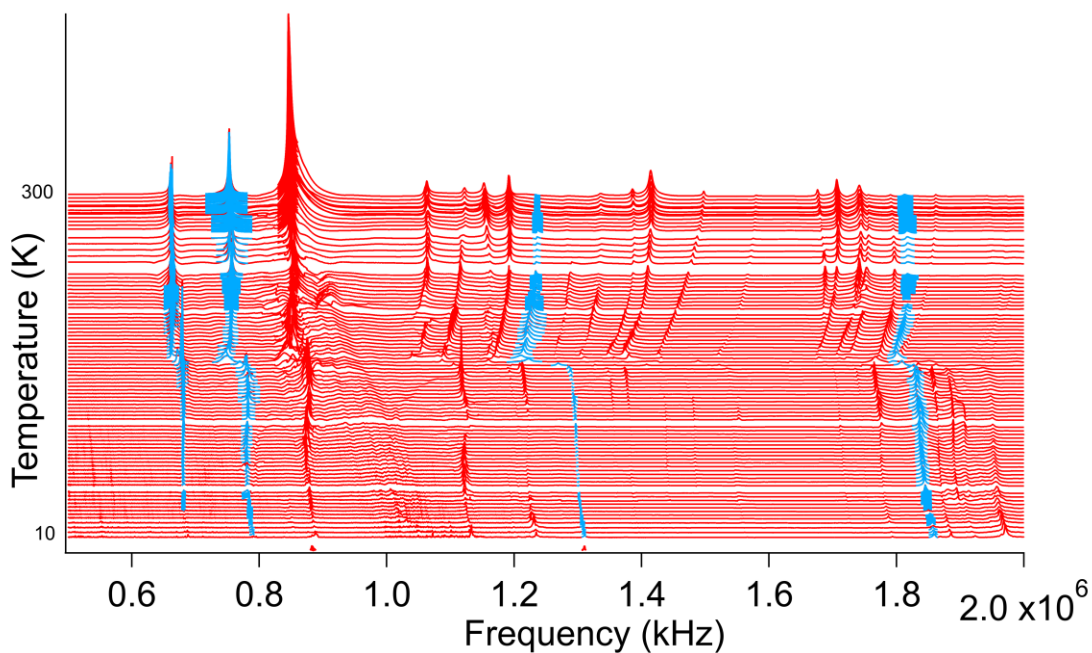
## 256 VII. RESONANT ULTRASOUND SPECTROSCOPY

257 Details of the instrument used to collect RUS data at low temperatures have been given  
258 elsewhere (McKnight et. al 2007). The sample sits lightly between two piezoelectric transducers  
259 in the RUS head, which is attached to the end of a stick and lowered into an Orange helium flow  
260 cryostat. In the present study, resonance spectra were collected in two automated cooling and  
261 heating sequences with steps of 30 K on cooling from room temperature to 10 K, and of between  
262 1K and 10K on heating from 10 K to 295 K. A settle time of 1200s was included to allow for  
263 thermal equilibration at each set point. Individual spectra contained 65,000 data points in the  
264 frequency range 100 kHz – 2 MHz, with a driving voltage of 25 V. One sequence was for a  
265 different piece of the original large 4C crystal and the second was for the 9.1 mg fragment of the  
266 5C crystal. Analysis of elastic and anelastic properties was undertaken by fitting selected peaks  
267 with an asymmetric Lorentzian function to give peak frequency,  $f$ , and width at half-maximum  
268 height,  $\Delta f$ . The natural resonances of a mm sized sample involve primarily shearing motions and  
269 the variations of  $f^2$  therefore reflect variations of different combinations of predominantly shear  
270 elastic constants, in this case of the single crystal. Acoustic dissipation is expressed in terms of the  
271 inverse mechanical quality factor,  $Q^{-1}$ , which, in a RUS experiment is usually specified as  $\Delta f/f$ .

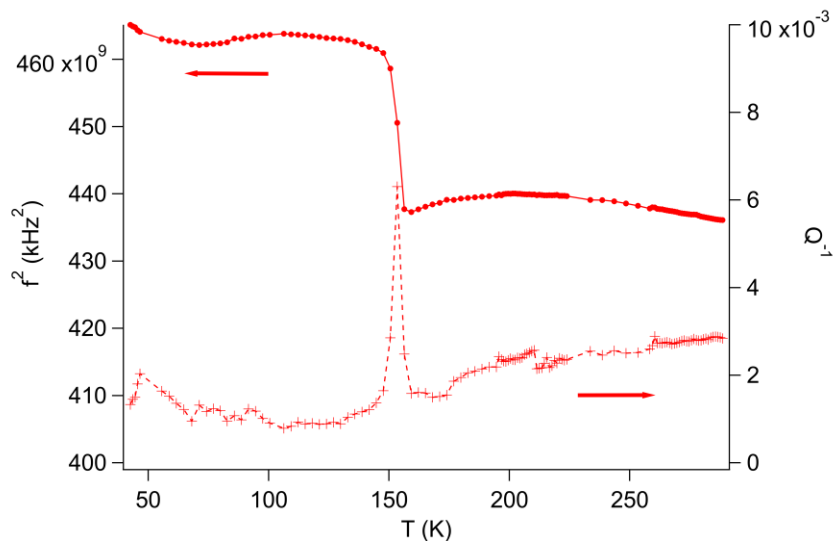
272 Figure 6 contains a stack of spectra from the heating sequence of the 5C crystal. The y-axis is  
273 amplitude, but the spectra have been offset in proportion to the temperatures at which they were



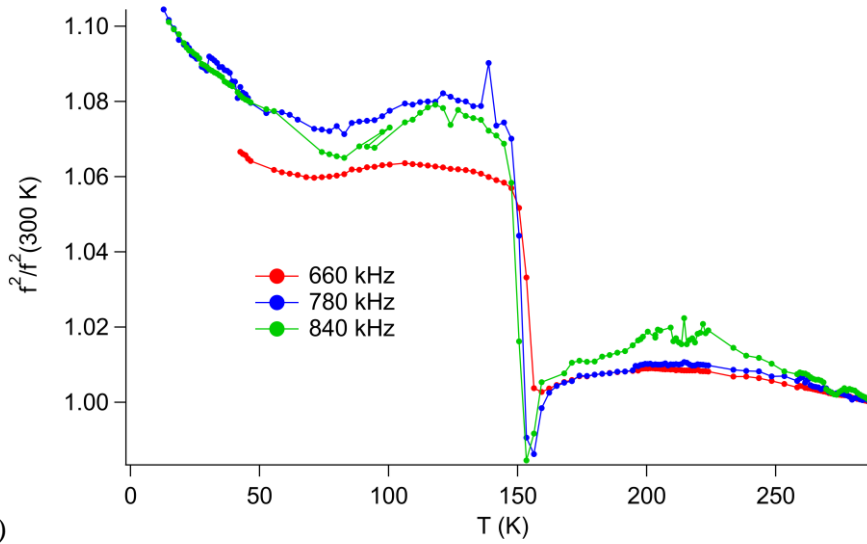
274 collected. The axis has then been relabelled as temperature in order to allow ready visualisation of  
275 the principal features of the elastic behaviour. All the resonances show the same pattern of  
276 reducing frequency (elastic softening) as the transition point is approached from above, followed  
277 by abrupt increases (elastic stiffening) at the expected transition temperature of  $\sim 155$  K. In other  
278 words, all the shear elastic constants of the crystal evolve in more or less the same manner. Blue  
279 curves are fits to individual peaks, and Figure 7a shows the variations of  $f^2$  and  $Q^{-1}$  for a peak near  
280 650 kHz. With falling temperature there is a trend of elastic softening by a few percent towards  
281 the transition point, followed by  $\sim 10\%$  stiffening in a narrow temperature interval between 150  
282 and 160 K. This temperature interval corresponds almost exactly with the temperature interval  
283 over which the anomaly in heat capacity extends (Fig. 3). The peaks generally remain quite sharp  
284 at all temperatures, with values of  $Q^{-1}$  in the vicinity of  $2 \times 10^{-3}$  apart perhaps from a slight increase  
285 in the vicinity of the transition point. The variation of  $f^2$  normalised to the room temperature value  
286 for three different peaks is shown in Figure 7b. Whilst the overall temperature dependence is  
287 similar the peaks behave slightly differently, as would be expected for a single crystal sample in  
288 which each resonance has a distinct contribution from the different elastic constants.  
289



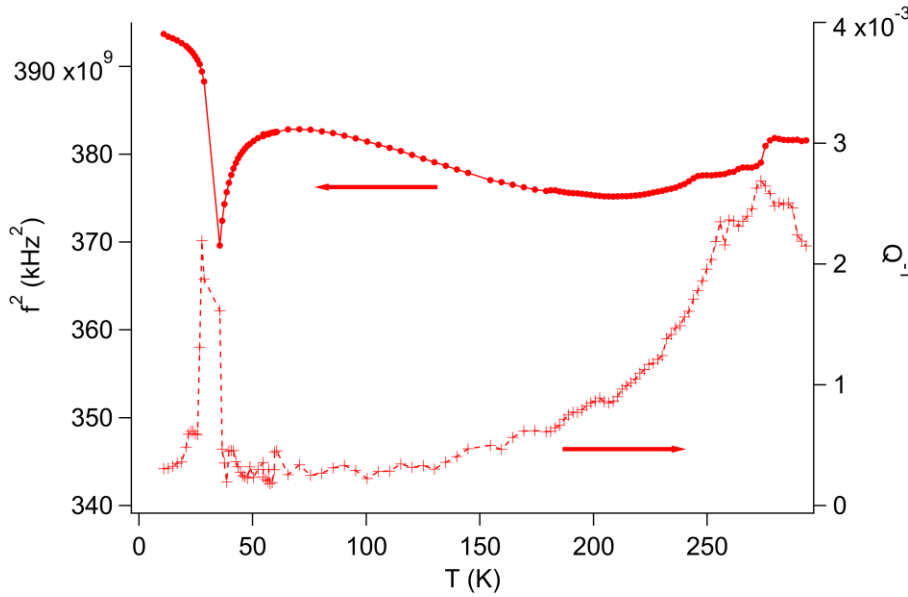
290  
 291 Figure 6. RUS spectra collected from the 9.1 mg piece of the 5C crystal in a heating sequence  
 292 from 10 to 295 K. The y-axis should be amplitude in volts, but the spectra have been offset in  
 293 proportion to the temperatures at which they were collected and the axis relabelled as temperature.  
 294 There is an abrupt change in frequencies of all the individual resonance peaks at the expected  
 295 transition temperature,  $\sim 155$  K. Fits to selected peaks are shown in blue.  
 296



297 (a)



298 (b)



299 (c)

300 Figure 7. (a) Temperature dependence of  $f^2$  and  $Q^{-1}$  for the single crystal of 5C pyrrhotite from  
 301 fitting of the resonance peak near 650 kHz and (b)  $f^2$  for three resonance peaks at 660 kHz, 780  
 302 kHz and 840 kHz normalised to the value at room temperature. (c) Temperature dependence of  $f^2$   
 303 and  $Q^{-1}$  for a single resonance with frequency near 620 kHz from a 4C pyrrhotite crystal cut from  
 304 the same original sample as was used to produce the 5C crystal. The Besnus transition is marked  
 305 by a minimum in  $f^2$  at  $\sim 36$  K. Crosses =  $Q^{-1}$ , right axis; filled circles =  $f^2$ , left axis.

306

307 Variations of  $f^2$  and  $Q^{-1}$  data from fits to a resonance peak near 620 kHz in spectra collected  
308 from the piece of original the 4C crystal are shown in Figure 7c. The crystal was cut from the same  
309 original sample as the piece that was converted to 5C. There are very obvious differences from the  
310 variations in elastic and anelastic properties that accompany the magnetic transition shown in  
311 Figure 7. In particular, softening by a few % with falling temperature is associated with a peak in  
312  $Q^{-1}$  at ~270 K. This turns into a trend of gradual stiffening followed by steep softening ahead of  
313 the Besnus transition, which is marked by a minimum at ~36 K.  $f^2$  values then recover steeply and  
314 there is a distinct peak in  $Q^{-1}$  immediately below the transition. The maximum change in  $f^2$  at the  
315 frequency of this resonance, ~620 kHz, is ~6%. Changes in elastic and anelastic properties  
316 accompanying the Besnus transition in 4C pyrrhotite are described in detail elsewhere (Haines et  
317 al 2019b).

318

## 319 **VIII. DISCUSSION AND CONCLUSIONS**

320 We have shown that 4C pyrrhotite can be transformed to 5C by annealing above the  
321 concomitant Néel and vacancy ordering temperature. On the basis of single crystal x-ray  
322 diffraction at room temperature we confirm that a model in space group  $Cmce$  can successfully  
323 explain the diffraction data. The low temperature structure has previously been refined  
324 successfully using a model in space group  $P2_1$  by Liles and deVilliers (2012). The Besnus  
325 transition is no longer observed and a new Morin-like spin-flop transition occurs at ~155 K  
326 instead. The magnetic properties of the 5C crystal are incompatible with impurities of 4C  
327 pyrrhotite or magnetite above the level of 1%. In addition, the heat capacity anomalies  
328 characteristic of the low temperature magnetic phase transitions in these two minerals were not  
329 observed. The 4C crystal from which the piece used in this study was cut showed no impurities  
330 above the level of detection in either powder XRD or electron microprobe measurements (Haines

331 et al. 2019b). Therefore, it is difficult to imagine any impurity other than the magnetite formed at  
332 the surface or ‘untransformed’ 4C pyrrhotite. We have carried out electron microprobe analysis  
333 on the 5C crystal and the sample is monophasic with a high degree of homogeneity. The impurity  
334 levels are on the border of detectability. The stoichiometry is homogeneous and works out to be  
335  $\text{Fe}_{9.2}\text{S}_{10}$  in good agreement with the single crystal refinement.

336 The most significant structural difference in comparison with the 4C structure is the change in  
337 vacancy ordering scheme which develops during cooling. Without specifying the ordering in  
338 detail, it is possible to assess the changes in structure and properties from the perspective of  
339 symmetry. If the reference structure at high temperatures is taken to be that of NiAs in space group  
340  $P6_3/mmc$ , the order parameter which gives rise to the 5C superstructure is most likely to have the  
341 symmetry of the active representation  $U_1(1/2,0,1/5)$  (Haines et al 2019a). A likely candidate for  
342 the magnetic order parameter has the symmetry of irreducible representation  $m\Gamma_5^+$ . The list of  
343 possible magnetic space groups that can result from this combination includes the previously  
344 reported crystallographic space groups  $Cmce$ ,  $P2_1/c$  and  $P2_1$  (Haines et. al 2019a). New magnetic  
345 and elasticity data have been interpreted here on the basis that 5C pyrrhotite is antiferromagnetic  
346 and that the magnetic transition at ~155 K is from one antiferromagnetic structure to another. In  
347 all of the reported space groups the moments can be aligned either in the plane perpendicular to  
348 the crystallographic  $c$ -axis of the parent or parallel to the  $c$ -axis. Across the  $\text{Fe}_{1-x}\text{S}$  phase diagram  
349 (Schwarz and Vaughan 1972) the 590 K transition is to a state in which the moments are in the  
350 plane perpendicular to the crystallographic  $c$ -axis. The low temperature spin-flop transition  
351 observed in troilite and the low temperature evolution of 4C pyrrhotite involve a rotation of the  
352 moments towards the  $c$ -axis.

353 Haines et. al (2019a) predicted that the magnetic transition in 5C would be an abrupt spin-flop  
354 transition. This is because for none of the experimentally reported structures is it possible to have

355 distortions which allow both  $m\Gamma_4^+$  and  $m\Gamma_5^+$  to have non-zero values. In other words, the moments  
356 are strictly confined to either the plane perpendicular to the  $c$ -axis or to the direction parallel to  
357 the  $c$ -axis. *Cmce* was reported for a crystal at room temperature with the  $P2_1$  structure being solved  
358 using data collected at 120 K. These two structures do not have a group-subgroup relationship so  
359 that a *Cmce* –  $P2_1$  transition is necessarily first order.

360 The spin-flop transition in 5C pyrrhotite is significantly different from the Besnus transition in  
361 4C pyrrhotite, as is seen clearly in differences between the two sets of elastic and anelastic data in  
362 Figure 7. As a function of temperature, the spin-flop transition is characterised by a steep increase  
363 in all the shear elastic constants over a narrow temperature interval, consistent with first order  
364 character. The low temperature structure is stiffer than the high temperature structure and has the  
365 same level of acoustic loss. In contrast, the Besnus transition occurs over a wider temperature  
366 interval, consistent with a second order transition between magnetic structures that do have a  
367 group-subgroup relationship. There is also a distinct peak in the acoustic loss that could relate to  
368 the development of a ferroelastic microstructure. Thus, the transition in the 5C crystal appears to  
369 be closely analogous to the magnetic transition to that seen in FeS at 440 K, which involves the  
370 same change in orientation of moments (Harihara and Murakami 1958, Andresen 1960, Sparks et.  
371 al 1960 and 1962, Andresen et. al 1967, Horwood et al 1976).

372 This combination of symmetry analysis and experimental data on the magnetoelastic behaviour  
373 shows that 5C pyrrhotite fits well into the wider picture for the diverse structures suggested for  
374 the system  $\text{Fe}_{1-x}\text{S}$  by Haines et al (2019a). The stable antiferromagnetic/ferromagnetic structure  
375 which appears across the solid solution at  $\sim 590$  K has moments aligned perpendicular to the  
376 crystallographic  $c$ -axis. At transition temperatures which reduce from  $\sim 440$  K with increasing  
377 concentration of vacancies, this gives way to another magnetic structure in which the preferred  
378 orientation of the moments is  $90^\circ$  away from the  $c$ -axis. Details of the precise magnetic structure

379 and possibilities for thermodynamically continuous pathways between the two magnetic states  
380 then depend on details of the vacancy ordering at different stoichiometries, as expressed in terms  
381 of order parameters with irreducible representations of the form  $U(1/2,0,1/x)$  where  $x$  is 3, 4, 5, 6  
382 or irrational, corresponding to the 3C, 4C, 5C, 6C and incommensurate phases of pyrrhotite. All  
383 these phases, apart from 3C, are expected to show one magnetic transition below room  
384 temperature. In 3C pyrrhotite the transition is expected to be above room temperature.

385

## 386 **IX. IMPLICATIONS**

387 The discovery of a low temperature spin-flop transition in the 5C superstructure of pyrrhotite  
388 must be seen within the context of the whole  $Fe_{1-x}S$  family. In this work we have shown that the  
389 behaviour of the 5C superstructure is consistent with a comprehensive group theoretical  
390 framework described in Haines *et al.* (2019a). The result fits with the 3C superstructure being  
391 ferrimagnetic at room temperature and, if the crystallographic space group of  $P3_121$  (Nakano *et*  
392 *al.* 1979; Keller-Besrest *et al.* 1983) is correct, with the magnetic moments aligned parallel to the  
393  $c$ -axis. A low temperature spin-reorientation transition like the Besnus transition must also be  
394 expected in the 6C superstructure. Thus, it seems that the spin flop transitions are all closely  
395 related and fundamentally due to the same underlying thermodynamic driving force.

396 An additional consideration relates to the fact that the 5C crystal studied in this work was the  
397 result of thermally cycling a 4C crystal through the concomitant vacancy ordering and  
398 ferrimagnetic ordering temperature, at 595 K, and then up to 875 K before cooling back to room  
399 temperature. To our knowledge, this is the first time that 5C pyrrhotite has been synthesised in  
400 this way.

401 Finally, our improved understanding of the nature of the vacancy ordering and related magnetic  
402 structures in the  $Fe_{1-x}S$  system means that an understanding of the microscopic mechanisms may

403 now be within reach for an important group of mineral sulphides. Further experiments and  
404 calculations should focus on the changes in electronic structure behind the changing magnetic  
405 anisotropy and its dependence on temperature, pressure and vacancy order.

406

#### 407 **ACKNOWLEDGMENTS**

408 The authors acknowledge funding from the Leverhulme Foundation, grant number RPG2016-  
409 298. Heat capacity and DC magnetic measurements were carried out using the Advanced Materials  
410 Characterisation Suite, funded by EPSRC Strategic Equipment Grant EP/M000524/1. RUS  
411 facilities in Cambridge were funded by grants to MAC from the Natural Environment Research  
412 Council of Great Britain (grant nos. NE/B505738/1 and NE/F17081/1) and from the Engineering  
413 and Physical Sciences Research Council (grant no. EP/I036079/1).

414

#### 415 **References**

- 416 Andresen, A. F., Hofman-Bang, N., Bak, T. A., Varde, E. & Westin, G. (1960). *Acta Chemica*  
417 *Scandinavica*, 14, 919–926.
- 418 Andresen, A. F., Torbo, P., Ostlund, E., Bloom, G. & Hagen, G. (1967). *Acta Chemica Scandinavica*, 21,  
419 2841–2848.
- 420 Bertaut, E. F. (1953). *Acta Crystallographica*, 6, 557-561
- 421 Besnus, M. J. & Meyer, A. J. P. (1964) *Proceedings of the International Conference on Magnetism*  
422 *Nottingham* 507-511
- 423 Charilaou, M., Kind, J., Koulialias, D., Weidler, P. G., Mensing, C., Löffler, J. F. & Gehring, A. U.  
424 (2015). *Journal of Applied Physics*, 118 083903
- 425 CrysAlisPro Software System, Rigaku Oxford Diffraction, (2018).
- 426 De Villiers, J. P. R. & Liles, D. C. & Becker, M. (2009). *American Mineralogist*, 94(10), 1405-1410.
- 427 De Villiers, J. P. R. & Liles, D. C. (2010). *American Mineralogist*, 95(1), 148-152.



428 Elliot, A. D. (2010). *Acta Crystallographica Section B*, 66(3), 271-279.

429 Fleet, M. E. (1971). *Acta Crystallographica Section B*, 27(10), 1864-1867.

430 Haines, C. R. S., Howard, C. J., Harrison, R. J. and Carpenter, M. A. (2019a) *Acta Crystallographica*  
431 *Section B* 75, 1208–1224

432 Haines, C. R. S., Volk, M., Dutton, S. E. and Carpenter, M. A. (2019b) *in preparation*

433 Haines, C. R. S., Lampronti, G. I. and Carpenter, M. A. (2019c) *in preparation*

434 Horwood, J. L., Townsend, M. G. & Webster, A. H. (1976) *Journal of Solid State Chemistry* 17 17-42.

435 Hunt, C. P., Moskowitz, B. M. and Banerjee, S. K. (2013). *Magnetic Properties of Rocks and Minerals.*  
436 *In Rock Physics & Phase Relations*, T. J. Ahrens (Ed.). doi:10.1029/RF003p0189

437 Keller-Besrest, F., Collin, G. & Comes, R. (1983). *Acta Crystallographica Section B* **39**, 296-303.

438 Kontny, A., De Wall, H., Sharp, T., & Posfai, M. (2000). *The American Mineralogist*, 85(10), 1416-  
439 1427.

440 Koto, K., Morimoto, N., & Gyobu, A. (1975). *Acta Crystallographica Section B*, 31(12), 2759-2764.

441 Liles, D. C. & De Villiers, J. P. R. (2012). *American Mineralogist*, 97(2), 257-261.

442 Martín-Hernández, F., Dekkers, M., Bominaar-Silkens, I., & Maan, J. (2008). *Geophysical Journal*  
443 *International*, 174(1), 42-54.

444 Mcknight, R., Carpenter, M., Darling, T., Buckley, A., & Taylor, P. (2007). *American Mineralogist*,  
445 92(10), 1665-1672.

446 Morimoto, N., Gyobu, A, Tsukuma, K, & Koto, K. (1975). *The American Mineralogist.*, 60(3-4), 240-  
447 248.

448 Nakano, A., Tokonami, M. & Morimoto, N. (1979). *Acta Crystallographica Section B*, 35(3), 722–724.

449 Nakazawa, H. & Morimoto, N. (1971). *Material Research Bulletin*, 6 345-358.

450 Posfai, M., Sharp, T., & Kontny, A. (2000). *The American Mineralogist*, 85(10), 1406-1415.

451 Powell, A., Vaqueiro, P., Knight, K., Chapon, L. & Sanchez, R. (2004). *Physical Review B*, 70(1).

452 Rochette, P., Gattacceca, J., Chevrier, V., Hoffmann, V., Lorand, J., Funaki, M., & Hochleitner, R.  
453 (2005). *Meteoritics & Planetary Science*, 40(4), 529-540.

- 454 Schwarz, E. J. & Vaughan, D. J., (1972). Magnetic Phase Relations of Pyrrhotite. *Journal of*  
455 *Geomagnetism and Geoelectricity*. 24. 441-458. DOI:10.5636/jgg.24.441.
- 456 Sheldrick, G. M. (1997). *shelxl97* and *shelxs97*. University of Göttingen, Germany.
- 457 Sheldrick, G.M., *Acta Crystallographica Section C* (2015), C27, 3-8.
- 458 Sparks, J. T., Mead, W., Kirschbaum, A. J. & Marshall, W. (1960). *Journal of Applied Physics*, 31(5),  
459 S356–S357.
- 460 Sparks, J. T., Mead, W. & Komoto, T. (1962) *Journal of the Physical Society of Japan* 17(Suppl. B-I)  
461 249-252.
- 462 Yamamoto, A. & Nakazawa, H. (1982). *Acta Crystallographica Section A*, 38(1), 79–86.